



POWER UP YOUR ANALYSIS

Application solutions for lithium-ion secondary battery analysis

Lithium-ion secondary batteries with high-energy density are emerging as a new energy source. Materials for analyzing battery contents such as positive electrode materials, negative electrode materials, separators, and electrolytes are vital in research development and quality control.

To improve battery characteristics and safety, it's essential to understand the internal state of the battery through multiple analyses. Explore our application solutions for lithium-ion secondary battery analysis that combine analytical instruments such as FT-IR, ICP-OES, GC/MS, and DSC.



Learn more at
www.perkinelmer.com/battery



Drying of NCM Cathode Electrodes with Porous, Nanostructured Particles Versus Compact Solid Particles: Comparative Study of Binder Migration as a Function of Drying Conditions

Julian Klemens,* Luca Schneider, Eike Christian Herbst, Nicole Bohn, Marcus Müller, Werner Bauer, Philip Scharfer, and Wilhelm Schabel

Porous, nanostructured $\text{Li}(\text{Ni}_x\text{Co}_y\text{Mn})\text{O}_2$ (NCM) achieves an improvement in the fast-charging capability and the durability of lithium-ion batteries. This improvement is attributed to an extended electrolyte–active material interface, where the electrochemical reactions take place and thus shorter diffusion paths inside the active material particles are necessary for charge transfer. Due to the porous particle morphology, new processing challenges arise compared to compact solid NCM. Herein, the properties of the slurries and the electrodes made of the two active materials and, in particular, the influence of the drying process on the binder distribution, are comparatively investigated. For the same composition of the slurries, a significantly lower dependence of adhesion force and discharge capacity at higher C-rates on the drying rate is shown when using porous, nanostructured particles instead of solid particles. Binder migration and thus an inhomogeneous concentration distribution of the polyvinylidene fluoride binder is less pronounced for these electrodes during faster drying. Cell tests with half cells show that after increasing the drying rate by more than 350%, the discharge capacity of the electrodes consisting of solid NCM is reduced by about 63% at 5C while for the electrodes made of porous material no reduction is measured.


1. Introduction

In 2019, about half of secondary battery use was covered by lithium-ion batteries and of these, one-third uses the cathode active material $\text{Li}(\text{Ni}_x\text{Co}_y\text{Mn})\text{O}_2$ (NCM).^[1] To further improve the performance of these cells, the chemical composition and crystal structure of the active materials can be optimized or the particle morphology improved. For the active material $\text{Li}(\text{Ni}_{1/3}\text{Co}_{1/3}\text{Mn}_{1/3})\text{O}_2$ (NCM111), morphologies such as preferentially oriented crystals in the particles,^[2] nanobrick morphology,^[3] one-dimensional hierarchical microrods,^[4] and hierarchically structured particles^[5–9] were investigated. The latter is achieved by forming secondary particles with open intraparticle pore structure from assembled primary particles. The advantages of such structures are higher rate capability and improved cycling stability, due to a larger interface between active material and electrolyte, smaller diffusion paths and lower mechanical stress during

cycling. By modifying the particle morphology of commercial compact materials in a few additional process steps, a comparison can be made between the commercial starting material and the produced structured material. This approach was applied in the work of Wagner et al.^[9] by grinding, spray drying and calcination commercial NCM111. The influences of the process parameters in the production of such structures on the electrochemical properties as a function of the particle morphology were investigated. The optimum sintering temperature was found to be between 850 and 900 °C, resulting in primary particle diameters of 350 and 550 nm. It is the optimum between the demands of the ionic conductivity of the primary particles and the electrical conductivity of the secondary particles. During the sintering process, the primary particles grow, which aggravates ion diffusion but increases the electrical conductivity due to sinter necks. The specific capacity was improved from 20 to 100 mAh g^{-1} at 10C for the original and the structured particles, respectively.^[9]

J. Klemens, E. C. Herbst, P. Scharfer, W. Schabel
Thin Film Technology (TFT)
Karlsruhe Institute of Technology (KIT)
76131 Karlsruhe, Germany
E-mail: julian.klemens@kit.edu

L. Schneider, N. Bohn, M. Müller, W. Bauer
Institute for Applied Materials (IAM) – Energy Storage Systems (ESS)
Karlsruhe Institute of Technology (KIT)
76144 Eggenstein-Leopoldshafen, Germany

 The ORCID identification number(s) for the author(s) of this article can be found under <https://doi.org/10.1002/ente.202100985>.

© 2022 The Authors. Energy Technology published by Wiley-VCH GmbH. This is an open access article under the terms of the Creative Commons Attribution License, which permits use, distribution and reproduction in any medium, provided the original work is properly cited.

DOI: 10.1002/ente.202100985

Cycling stability studies with extensive electrochemical impedance spectroscopy and post-mortem analyses on electrodes with commercial and porous particles were carried out by Dreizler et al.^[10] Despite the higher specific surface area, the charge transfer resistance of the cathode is significantly lower and more stable for porous particles after a short run-in period than for compact particles, where this resistance increases during cycling. Fragmentation of the compact particles could lead to this increase. A buffer space inside the secondary particle, as is the case with porous particles, leads to less mechanical stress and prevents cracking in the particles.^[11] In contrast, the contact resistance between the current collector and the electrode layer increases slightly over the cycles for the compact particles, while this resistance almost doubles for the porous particles. Postmortem SEM images show interparticle cracks in the electrode with porous particles that can lead to this increase in contact resistance.^[10]

Müller et al.^[12] showed that electrodes containing a porous NCM material have comparatively lower adhesion strength values. The reason for the low adhesion forces within the electrode and to the current collector is that part of the binder has penetrated into the secondary particles and is therefore not available for adhesion. The influence of the penetration of the binder into the secondary particles on drying and the distribution of the components has not yet been investigated. An investigation of the component distribution during drying is necessary to further optimize the electrodes with porous particles and to further exploit their potential.

An improvement of the electrode adhesion can be achieved by appropriate formulation and optimizations during calendaring, which was investigated by Müller et al.^[12] Increasing the binder content in the dried electrodes from 8.25 to 11.89 vol% resulted in a slight increase in the adhesion force to just over 10 N m^{-1} . Porous NCM showed a high dry film porosity of $\approx 70\%$, which is disadvantageous for the volumetric energy density. By calendaring, the porosity could be reduced to $\approx 40\%$ without any fractures of the electrodes. Interestingly, also crack-free deformation of the porous secondary particles was observed, possibly attributed to the binder accumulation within the particles.^[12] Compression of the electrode during calendaring increased the adhesion force

of the electrode made of porous particles to 25 N m^{-1} at 45% porosity. In contrast, the adhesion force of the electrodes made of solid NCM was still higher with $\approx 35 \text{ N m}^{-1}$. Furthermore, the influence of calendaring on the macrostructure of compact and porous particles was found to be different. For electrodes with compact particles, compression led to a reduction in porosity between the particles and a slight reduction in pore diameter. For electrodes with porous particles, the porosity between the particles (interparticle porosity) disappeared, while the porosity within the particles (intraparticle porosity) remained.^[12] Long-term cycling, however, showed a state of health (SOH) of about 96% for porous and 64% for compact particles after 1100 cycles, despite reduced adhesion.^[12]

1.1. Microstructure Formation during Drying of Battery Electrodes

The microstructure formation of battery electrodes takes place in distinct steps during drying, while the drying conditions influence the properties of the electrodes.^[13–20] The various steps during drying are illustrated for graphite anodes by Jaiser et al.^[13,18] using five stages of the drying film (**Figure 1**).

Figure 1a–c: During the drying process and with progressive evaporation of the solvent, the wet film thickness of the electrode layer decreases. After a short time, a stationary state is reached, in which the drying rate remains constant (constant rate period) and the temperature in the drying film adjusts to the constant wet bulb temperature. As long as the electrode surface sufficiently stays wet by capillary transport processes, the electrode dries with constant drying rate (Equation (1)).^[15,21–24]

$$\dot{m}_s = \tilde{M}_s \tilde{\rho}_g \beta_{s,g} \ln \left(\frac{1 - \tilde{y}_{s,\text{dryer}}}{1 - \tilde{y}_{s,\text{surface}}} \right) \quad (1)$$

The drying rate or mass transfer in the gas phase depends in particular on the mass transfer coefficient $\beta_{s,g}$, the molar solvent loading of the supplied drying air $\tilde{y}_{s,\text{dryer}}$ and the molar solvent loading at the interface between the gas phase and the solvent $\tilde{y}_{s,\text{surface}}$. Thus, the drying rate for a solvent can be adjusted by

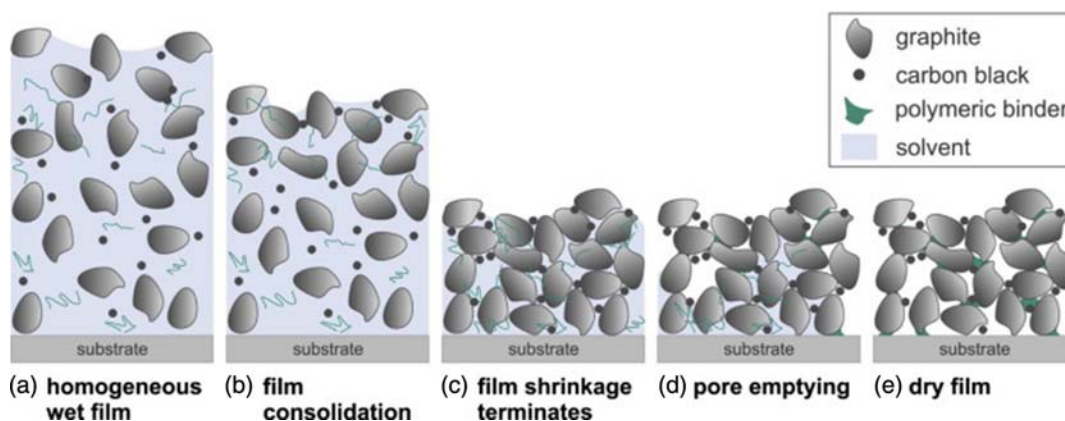


Figure 1. Schematic illustration of the drying of a particulate film for the production of a battery electrode. a) At the beginning of drying, the components are homogeneously distributed in the slurry. b,c) Due to drying, the film shrinks and the particles approach each other until the final porosity is reached. d) Pore emptying takes place. e) Dry film or electrode. Reproduced with permission.^[13] Copyright 2017, Elsevier.

the temperature, the flow conditions, and the solvent loading of the drying air. The mass transfer coefficient β can be calculated by the Lewis analogy and the connection to the heat transfer coefficient.^[15] The heat transfer coefficient, in turn, is determined by geometric size of the dryer, flow conditions and temperature.

The solid particles approach each other during drying (Figure 1c) and as soon as no further approach can take place, the final porosity $\varepsilon_{\text{electrode}}$ of the electrode (Equation (2)) is reached.

$$\varepsilon_{\text{electrode}} = 1 - \frac{m_{\text{electrode}}}{\rho_{\text{dry mixture}} \cdot h_{\text{dry}}} \quad (2)$$

The electrode porosity depends on the area weight of the electrode $m_{\text{electrode}}$, the density of the dry components $\rho_{\text{dry mixture}}$ in the coating and the average layer thickness h_{dry} . In some other publications, it has been shown that the electrode porosity is not affected by increasing the drying rate with increasing drying temperature.^[18,19,25]

At the point where film shrinkage terminates and the final electrode thickness is reached, a capillary network with solvent-filled pores has formed. Jaiser et al.^[14] investigated the microstructure formation of graphite anodes with a polyvinylidene fluoride (PVDF) binder system and N-Methyl-2-pyrrolidone (NMP) as solvent during drying and postulated a homogeneous distribution of the active material particles during the drying process. Furthermore, the pore emptying mechanism during drying was investigated (Figure 1d). For these electrodes, the surface of the film remained wetted and the drying rate remained constant even after the end of film shrinkage, which indicates for the occurrence of capillary transport processes to the surface of the electrode. The reason for this is the heterogeneous pore size distribution in the particulate electrode, resulting in high capillary pressure differences.^[13,14,22,26,27] According to the Young-Laplace equation, the capillary pressure of a single capillary is reciprocally dependent on the radius.^[22] The smaller the solvent transporting capillaries, the greater the capillary pressure. For connected capillaries, this means that due to the difference in capillary pressure, the larger pores empty in favor of the smaller ones. In the further progress of drying, the smaller pores remain filled with solvent for a longer period of time in average.^[22,26]

According to Pfaffmann et al.,^[17] pore emptying can already begin before the end of film shrinkage and, thus, before the final porosity of the electrode is reached. As soon as capillary pressure differences within the particulate network are large enough, transport processes take place (Figure 1d). The capillary liquid transport within the electrode because of progressive drying can lead to the binder being transported towards the electrode surface. The result is the formation of a binder concentration gradient in the dried electrode, which is a much discussed problem in the manufacture and use of battery electrodes.^[14,16,18,28–33] This binder migration was also confirmed when using a carboxymethyl cellulose (CMC) and styrene-butadiene rubber (SBR) binder system for application in high energy anodes for lithium-ion batteries.^[15]

At higher drying rates and, thus, shorter drying times, the binder concentration increases at the top of the electrode and decreases near the substrate, reducing adhesion and negatively influencing mechanical properties.^[13,15,18,34,35] Faster drying and the resulting capillary transport in the electrode accelerate the migration of the binder. In addition, it is discussed in the

literature that a shortened drying time might allow less time for concentration equilibration through Brownian molecular motion. At low drying rates, these diffusion processes may partially compensate for the concentration gradients, which could explain the less pronounced binder migration.^[14,15,18] The latter could be confirmed in simulations for a PVDF/NMP system.^[29]

In addition, the resulting concentration gradient of the binder leads to an inhomogeneous distribution of the carbon black particles and to an increase in electrical resistance, due to reduced electrical contact between the active material and the conductive additives as well as the formation of insulating binder layers and an accompanying increase in overpotential and, therefore, a decrease in specific capacitance, especially at higher currents.^[17,18,20,34–36]

If capillary transport fails to maintain a wet electrode surface, the menisci retreat into the porous structure and the electrode dries out further. Consequently, the evaporation of the solvent no longer takes place at the upper surface but in the porous structure. The drying rate decreases due to the additional mass transfer resistance within the electrode (falling rate period).^[14,22,23,26,37]

This work focuses on the effects of nanostructuring active particles for NCM cathodes on electrode production. It has to be clarified whether the penetration of the binder into the particles has an influence on the processing. In particular, the dependence of the electrode properties on the drying conditions for solid particles and porous, nanostructured particles is investigated. The relationship between drying conditions and the distribution of binder concentration is compared via the adhesion force, resistivity, component distribution and electrochemical behavior. The study of drying porous electrodes with porous particles is not known in the literature and provides new approaches to extend the previous state of the art regarding the drying mechanism of electrodes.

2. Results and Discussion

The aim of this study is to investigate the drying of cathode slurries with porous, structured particles and to understand the mechanisms of binder migration compared to slurries using solid material.

2.1. Particle Systems

The porous, structured NCM111 (NCM-P) was prepared from the compact solid material NCM111 (NCM-C) to investigate the influence of process conditions on electrode fabrication characteristics and electrode properties. For this purpose, various process steps for the treatment of the particles were carried out in this work, as described in Wagner et al.^[9] The initial material was ground in a stirred ball mill to an average particle size of 297 nm and then suspended in water. The suspension was processed in a spray dryer to obtain spherical secondary particles. To increase the mechanical stability of the particles, a calcination process in hot air was carried out at 850 °C for a duration of 5 h. During this heat treatment, a gradual sintering of the primary particles takes place.

The secondary particles of the original NCM-C have an irregular, granular particle shape with a rough surface (Figure 2).

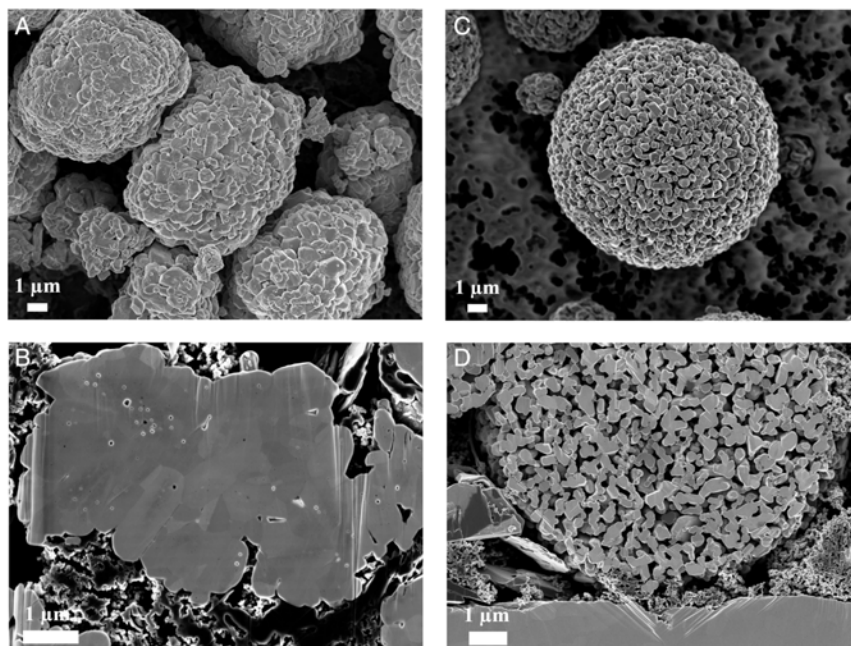


Figure 2. SEM images of the secondary particles of the two active materials for the cathodes NCM-C (A, B) and NCM-P (C, D). The NCM-C secondary particles are granular and have a rough surface. In addition, they show a compact structure in which the primary particles (crystal grains) are hardly recognizable. The inner structure of NCM-P particles is porous, and the particles have a rounded shape due to spray drying.

Table 1. Overview of the particle properties of the investigated cathode material.

Abbreviation	Primary particle diameter [μm]	Secondary particle diameter [μm]	Specific surface area [$\text{m}^2 \text{g}^{-1}$]	Pure density [g cm^{-3}]	Secondary particle porosity [%]
NCM-C ^[12]	0.770	7.3	0.4	4.52	–
NCM-P	0.434	10.0	2.9	4.70	47.6

In contrast, the secondary particles of NCM-P have an almost spherical shape due to the spray drying process.

The average secondary particle diameters of the two materials are in a comparable range of 7.3 μm (NCM-C) and 10 μm (NCM-P), respectively. The secondary particles of NCM-P exhibit an internal porosity of 47.1% due to an open-structured arrangement of the primary particles with a particle diameter of 0.434 μm . Despite the slightly larger average secondary particle diameter, the internal porosity of the particles increases the specific surface area (BET) by 625% from 0.4 to 2.9 $\text{m}^2 \text{g}^{-1}$. An overview of the different particle properties is shown in Table 1.

2.2. Slurry Composition and Flow Behavior

Rheological investigations allow an insight into the flowability of the slurry, which is crucial for the coating process and the process stability.^[36,38–40] To investigate the influence of particle morphology on the electrode production process, slurries were prepared using the same composition and procedure, and the flow behavior was characterized. An overview of the composition of the slurries used for these studies is shown in Table 2.

Table 2. Composition of the cathode slurries.

Abbreviation	NCM [wt%]	Graphite [wt%]	CB [wt%]	PVDF [wt%]	Solids [wt%]
NCM-C/NCM-P	89,29	3,57	3,57	3,57	50,5

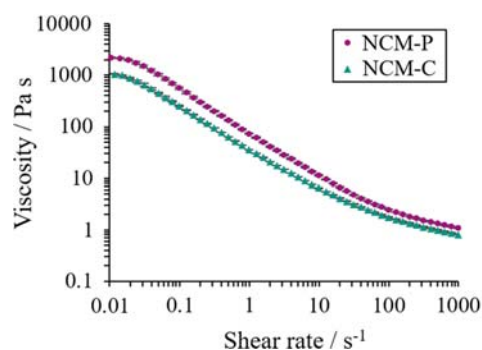


Figure 3. Dynamic viscosity of cathode slurries with porous, structured NCM-P (red dots) and solid NCM-C (green triangles) as a function of shear rate at a temperature of 25 °C.

The flow behavior was determined by measuring the viscosity as a function of shear rate for both slurries at a constant temperature of 25 °C (Figure 3).

The slurries show high viscosities in the range of the investigated low shear rate of 0.01 s⁻¹ of 1060.0 ± 8.2 Pa s (NCM-C) and 2203.3 ± 54.4 Pa s (NCM-P), respectively. Both viscosity curves show a strong shear thinning behavior, down to 0.82 ± 0.01 Pa s (NCM-C) and 1.08 ± 0.01 Pa s (NCM-P) for a shear rate of 1000 s⁻¹, respectively. In the range of the shear rate from ≈0.1 s⁻¹ to ≈10 s⁻¹, both systems show an exponential decrease of the viscosity. At low shear rates (0.01 s⁻¹), the viscosity of NCM-P is 107% higher, and as the shear rate increases, the viscosities approach each other. At a higher shear rate of 1000 s⁻¹, the viscosity of NCM-P is still 30% higher. Throughout the shear rate range considered, the viscosity curve of the NCM-P slurry is higher than the viscosity of the NCM-C. Since the solids content and composition are the same for both slurries, the difference in viscosity must be due to the different particle properties of NCM-C and NCM-P. For particle sizes of the same order of magnitude, it can be assumed that particle shape and distribution have less influence. A major difference in the particle morphologies of both particle systems is the larger specific surface area and the internal porosity of the secondary particles of NCM-P. As also discussed by Müller et al.,^[12] it would be conceivable that during slurry preparation the solvent NMP, including the dissolved PVDF binder, absorbs into the open-pore structure of the particles. A schematic illustration of the processes during slurry preparation is shown in Figure 4.

Due to the assumed high capillary absorption capacity caused by the small capillary sizes within the particles, solvent infiltration into the particles occurs. Especially at low shear rates, the infiltrated liquid can be considered as a stationary phase. Consequently, the solvent infiltrated into the particles would no longer affect the flow behavior of the slurry, and the effective solids content in the slurry around the porous particles would increase. Since the binder is dissolved in the solvent, it is also assumed that the binder concentration in the pores of the particles and in the pore network between the particles is the same at the beginning of drying and corresponds to the initial concentration. Due to the porosity of the particles of almost 50%, the relevant volume fraction of the active material in the slurry increases by

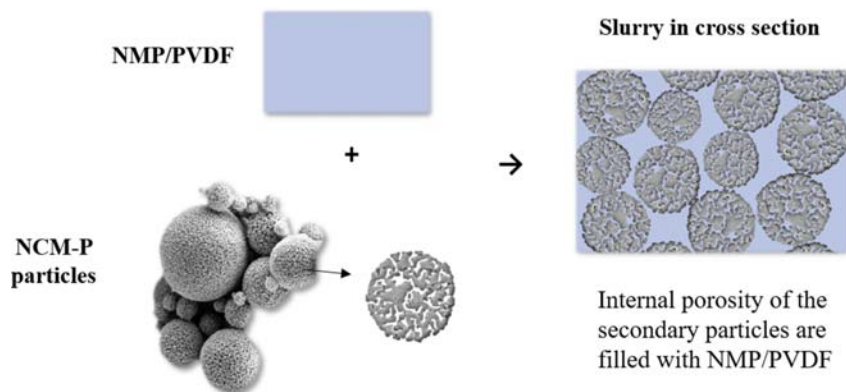


Figure 4. Schematic illustration of the slurry with porous, nanostructured particles and the penetration of the solvent with the dissolved binder into the pore structure of the particles. For illustrative purposes, the conductive additives have not been shown.

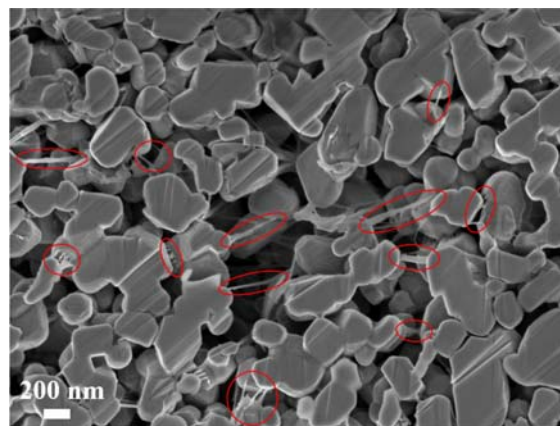


Figure 5. SEM cross-sectional image of a dried porous, nanostructured cathode particle with visible PVDF fibers and bridges between the primary particles. The binder causes additional crosslinking between the primary particles.

a factor of about two. Thus, there are more particles in a volume element, the internal friction in the slurry increases, and consequently the viscosity increases over a wide shear rate range.

SEM cross-sectional images of the porous secondary particles after drying the slurry with the NCM-P particles reveal the existence of PVDF-binder bridges within the particles and, therefore, support the hypothesis of NMP-PVDF penetration into the secondary NCM-P particles during slurry preparation (Figure 5).

2.3. Adhesion

The adhesion force, measured by 90° peel tests, provides an indirect quantification of the binder migration and the mechanical properties of electrodes.^[15,35–37] The drying rate is varied for the same heat transfer coefficient by adjusting the isothermal drying temperature. For this purpose, the slurry is dried convectively via drying nozzles in a batch dryer with a heated plate. Homogeneous drying is achieved by periodically moving the layer back and forth under the dryer. The isothermal drying temperatures are calculated according to Equation (2) and can be found in Table 3.

Table 3. Overview of the drying rate and the calculated isothermal drying temperature with a constant heat transfer coefficient of $80 \text{ W m}^{-2} \text{ K}^{-1}$.

Drying rate [$\text{g m}^{-2} \text{ s}^{-1}$]	Isothermal drying temperature [$^{\circ}\text{C}$]
0.75	61
1.50	73
1.70	75
2.00	79
3.50	85

The electrodes were dried at different drying rates and the dependence of the adhesion force on the drying rate was measured (Figure 6). Table 4 shows an overview on the dry film thicknesses, area weights and the layer porosities of the tested electrodes.

As the drying rate increases from 0.75 to $2 \text{ g m}^{-2} \text{ s}^{-1}$, the adhesion force of NCM-C electrodes decreases from 27.70 ± 1.44 to $12.30 \pm 0.88 \text{ N m}^{-1}$. This decrease corresponds to an almost linear reduction in the adhesion force of $\approx 56\%$. When the drying rate is further increased from 2 to $3.5 \text{ g m}^{-2} \text{ s}^{-1}$, the adhesion force decreases less than in the first section, to $7.71 \pm 0.8 \text{ N m}^{-1}$. Overall, the adhesion force decreases by $\approx 72\%$ in the range of drying rates considered.

The electrodes with NCM-P particles show a significantly lower adhesion level than NCM-C. For drying rates of 0.75

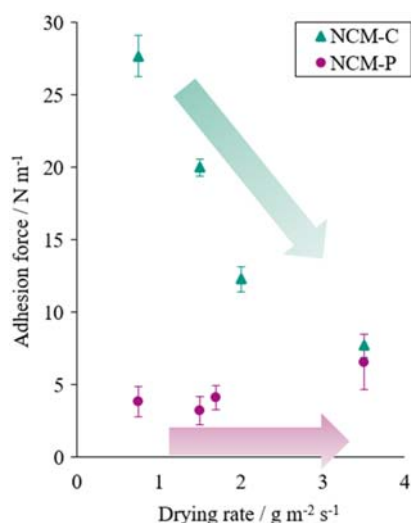


Figure 6. Adhesion force (90° peel test) of non-calendered cathodes with NCM-C (green triangles) and NCM-P (red dots) as a function of drying rate at a constant heat transfer coefficient of $80 \text{ W m}^{-2} \text{ K}^{-1}$. Drying rate is varied via the calculated isothermal drying temperature.

Table 4. Overview of the non-calendered electrodes: dry film thickness, area weight and electrode porosity.

Abbreviation	Dry film thickness (noncalendered) [μm]	Area weight [g m^{-2}]	Electrode porosity [%]
NCM-C	78.4 ± 1.4	153.6 ± 3.6	50.6 ± 1.1
NCM-P	79.3 ± 3.2	104.6 ± 3.8	67.7 ± 1.0

and $1.5 \text{ g m}^{-2} \text{ s}^{-1}$, the adhesion force is in the range of $3.73 \pm 0.47 \text{ N m}^{-1}$. For a drying rate of $3.5 \text{ g m}^{-2} \text{ s}^{-1}$, a slightly higher adhesion force of 6.57 N m^{-1} is observed, although here the standard deviation of 2.34 N m^{-1} is relatively high in comparison to the one of NCM-C. Overall, the standard deviations of the adhesion forces are higher in percentage for NCM-P than for NCM-C, thus, a dependence of the adhesion force on the drying rate cannot be detected. The reduction in adhesion force by increasing the drying rate with an increase in isothermal drying temperature for NCM-C is in good accordance with experimental studies on drying of graphite anodes for LIB with CMC/SBR and also with PVDF systems.^[15,18,19] As the drying rate increases, the capillary transport rate increases. In addition, the drying time is shortened, which means that less time is available for concentration equalization of PVDF gradients by diffusion. Second, increasing the drying temperature leads to a lower viscosity of the binder solution, which reduces the capillary pressure losses and thus increases the capillary transport processes and thus binder migration. As a result, there is a depletion of the binder near the substrate, which decreases the adhesion force.

The NCM-P electrodes show an overall lower adhesion force. The rheological data and Figure 5 show the infiltration of NMP/PVDF into the particles. As a result, the effective binder to solid particle ratio in the slurry and in the capillary network around the particles decreases. Since the binder is not available for adhesion to the substrate, this could explain the overall low adhesion for the NCM-P electrodes. The result that the adhesion force for the slurry composition used is approximately constant could indicate that the binder has a different mobility. It would be conceivable for the binder to take a stationary and a mobile fraction for both particle systems during drying.^[41] During drying, the stationary fraction is not transported by capillary transport, but remains in the same position until the end of drying. Thus, it is possible that the surface of the active material particles and the carbon additives are covered by part of the binder and remains covered to the same extent.

Accordingly, the mobile binder fraction is the fraction which can migrate to the surface, which results in the observed binder concentration gradient after drying and, especially after faster drying. The stationary binder fraction could be responsible for a lower limit of adhesion force. In the case of the NCM-P system, less mobile binder is available, since a significant amount of binder is trapped inside the porous particles. It would be conceivable that the stationary part of the binder is similar for both material systems, only for the NCM-C system the mobile fraction of the binder is more and more migrating to the electrode surface with increasing drying rate, while the amount of mobile binder in the NCM-P system is already low from the beginning and not significantly contributing to the measured adhesion, regardless of any migration at different drying rates. This could lead to similar adhesion forces for both material systems at very high drying rates, where the adhesion might be only due to the stationary binder fraction, as indicated by the measurement for high drying rates of $3.5 \text{ g m}^{-2} \text{ s}^{-1}$.

Another aspect that has not been further investigated here is that particle size and shape can play a role in their adhesion to the substrate. The small granular particles of the NCM-C could have a higher average adhesion force to the substrate than the larger round NCM-P particles. If we would assume that the binder is

evenly distributed over the BET surface of the active material and the conductive additives,^[42,43] such a binder layer decreases in thickness with increasing specific surface area of NCM-P. For a certain small thickness or small amount of binder relative to the surface, this could result in a lower adhesion force. This assumption may no longer be valid, especially if a concentration gradient of binder occurs in the electrode due to drying and capillary transport. In particular, this would not explain the influence of the drying rate on the adhesion force.

2.4. Resistivity

Electrical resistivity was determined as a function of the drying rate (Figure 7).

Due to the higher porosity, the resistivity of NCM-P electrodes is significantly higher than that of NCM-C. The measured values of the resistivity in the low drying rate range are in good agreement with the studies of Müller et al.,^[12] where comparable drying conditions were used. The electrodes of both materials show an increase in resistivity with increasing drying rate. The resistivity of NCM-P is between $37.0 \pm 2.87 \Omega\text{m}$ ($0.75 \text{ g m}^{-2} \text{ s}^{-1}$) and $73.92 \pm 3.94 \Omega\text{m}$ ($3.5 \text{ g m}^{-2} \text{ s}^{-1}$), and of NCM-C between $3.64 \pm 0.31 \Omega\text{m}$ ($0.75 \text{ g m}^{-2} \text{ s}^{-1}$) and $14.13 \pm 0.60 \Omega\text{m}$ ($3.5 \text{ g m}^{-2} \text{ s}^{-1}$). Therefore, the increase in resistivity with increasing drying rate of NCM-P is about 100% and of NCM-C is about 288%.

The electrical conductivity depends on the conductivity of the active and inactive materials as well as on the distribution and contact resistance of the components. Increasing resistivity often indicates an increasing inhomogeneity of the additive distribution in the microstructure within the electrodes. Jaiser et al.^[18] postulated and Pfaffmann et al.^[17] found that with increasing drying rate for thick electrodes, the conductive carbon black migrates during drying of graphite anodes in addition to the binder. A similar behavior can be expected for cathodes. The accumulation of carbon black at the top of the electrode will cause the formation of a depleted area in lower layers. By measuring the resistivity planar between

current collector and top of the electrode, the sequential arrangement of the layers should lead to an increase in resistivity. Müller et al.^[16] and Jaiser et al.^[18] showed an accumulation of PVDF on the surface of graphite anodes as a consequence of a stronger binder migration at higher drying rates. For the applied resistivity measuring method, an accumulation of binder on top of the electrode would lead to an increase in the measured electrical contact resistance.

The higher increase in resistivity with increasing drying rate of NCM-C compared to NCM-P could therefore be attributed to a different binder distribution. In the case of NCM-P, some binder is located in the pores of the secondary particles (see Figure 5) increasing the stationary fraction of the binder, which remains at place during drying. As a result, only a smaller binder accumulation will arise compared to NCM-C, and with the same binder content the increase in resistivity will be comparatively smaller.

2.5. Influence of Calendering on Electrical Resistivity

Both cathode systems were calendered to a porosity of $\approx \epsilon = 40\%$ and the resistivities were measured (Figure 8). Due to the higher initial porosity, NCM-P required a higher compression factor compared to NCM-C.

Calendering leads to a decrease in resistivity for both cathode systems, which is in good agreement with the results of Müller et al.^[12] For the lowest and the highest drying rate, the resistivity is reduced by 95% in each case of NCM-P. For NCM-C the resistivity decreases by 78% ($0.75 \text{ g m}^{-2} \text{ s}^{-1}$) and 94% ($3.5 \text{ g m}^{-2} \text{ s}^{-1}$). This is because of the improved contacting and percolation due to compaction of the conductive additives between the active material.^[12] An influence of the drying rate can no longer be identified for NCM-C after calendering. The cathode system of NCM-P, on the other hand, shows an increase in the resistivity with the drying rate even after calendering. Between the lowest and the highest drying rate, the resistivity is twice as large for the calendered electrodes. It is conceivable that due to the higher

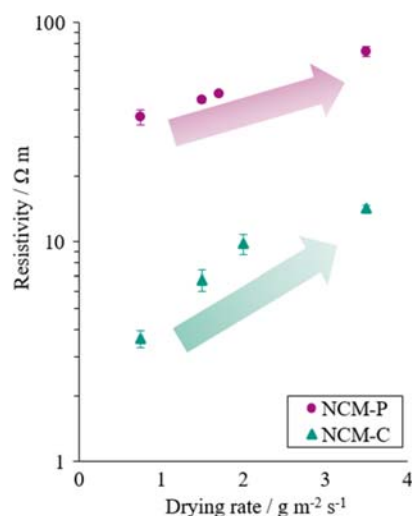


Figure 7. Resistivity of non-calendered cathodes with NCM-C (green triangles) and NCM-P (red dots) as a function of drying rate at a constant heat transfer coefficient of $80 \text{ W m}^{-2} \text{ K}^{-1}$.

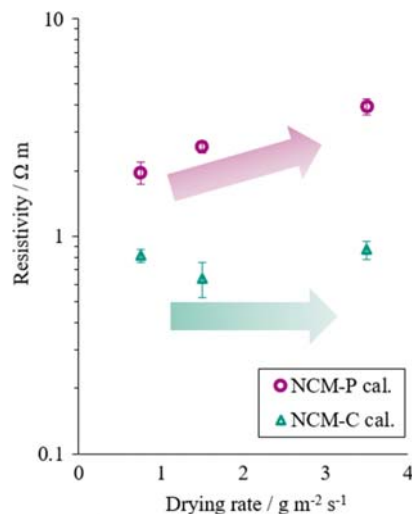


Figure 8. Resistivity of calendered cathodes ($\epsilon \approx 40\%$) with NCM-C (green triangles) and NCM-P (red dots) as a function of drying rate at a constant heat transfer coefficient of $80 \text{ W m}^{-2} \text{ K}^{-1}$.

compression of the electrodes, minor inhomogeneities in the binder concentration distribution, which can occur at higher drying rates with NCM-P electrodes, become more significant.

2.6. Component Distribution Depending on Drying and Particle Properties

To further quantify the measured influences of mechanical and electrical behavior as a function of drying rate, energy-dispersive X-ray spectroscopy (EDS) analyses were carried out. Measurements were made on cross sections of calendered cathodes ($\epsilon \approx 40\%$) dried at the lowest drying rate $0.75 \text{ g m}^{-2} \text{ s}^{-1}$ and the highest drying rate $3.5 \text{ g m}^{-2} \text{ s}^{-1}$. **Figure 9** shows the carbon and fluorine distribution for NCM-C depending on the drying rate.

Figure 9 shows a homogeneous distribution of NCM particles for both drying rates. The active material consists of lithium, nickel, manganese, cobalt, and oxygen, but does not contain carbon or fluorine and is therefore represented by dark areas surrounded by carbon additives (Figure 9A,C) and fluorine (Figure 9B,D). Locally distributed, differently sized accumulations and agglomerates of conductive graphite and conductive carbon black are present at both drying rates. A possible migration of conductive additives cannot be confirmed based on these EDS images by simple optical observation.

The fluorine distribution shows an accumulation within the compact, closed NCM-C particles for both drying rates. The reason for this is an overlay of EDS spectra of fluorine with manganese and cobalt, resulting in a virtually high fluorine concentration (so-called “fluorine noise”).^[12] Nevertheless, qualitative differences in the fluorine distribution over the layer height and depending on the drying conditions can be detected. The fluorine concentration, and thus the PVDF binder, is primarily located together with the conductive additives due to the high specific surface area.^[42–44]

A homogeneous distribution is observed at the lower drying rate. For the higher drying rate, there is a reduction at the bottom (phase boundary near the substrate) and an increase at the top of the electrode.

The carbon distributions of NCM-P also show that the NCM particles are clearly separated and do not contain carbonaceous material inside (see **Figure 10A,C**).

Carbon forms a network around the NCM-P particles in this case too. The conductive additive accumulations are smaller per area for NCM-P compared to NCM-C because the electrodes are more compacted. However, there are also locally distributed accumulations and agglomerates of conductive graphite and conductive carbon black of different sizes. A difference in the conductive additive distribution between high and low drying rate cannot be detected in the EDS images. Considering the fluorine distribution, individual NCM-P active material particles can hardly be distinguished, since the fluorine concentration detected in the particles is significantly larger compared to the contribution of fluorine noise within the NCM-C particles. The reason for this is the binder accumulation in the porous secondary particles. The fluorine shows a uniform distribution over the entire cross section for the lower drying rate. The affinity of binder to conductive additives appears to be less pronounced for both drying rates since the carbon distribution is hardly recognizable in the fluorine mapping. An increase in drying rate also leads to an increase in binder concentration at the top of the electrode. This suggests that the drying process in NCM-P is also dominated by pore emptying of the outer, larger pore network (interparticle pore network) through capillary transport effects. However, when looking at the average fluorine concentrations within discrete shells of the secondary particles of NCM-P (**Figure 11**), no significant change in binder concentration within the particles is evident (**Table 5**), implying that there is no binder migration from within the secondary particles to the outside.

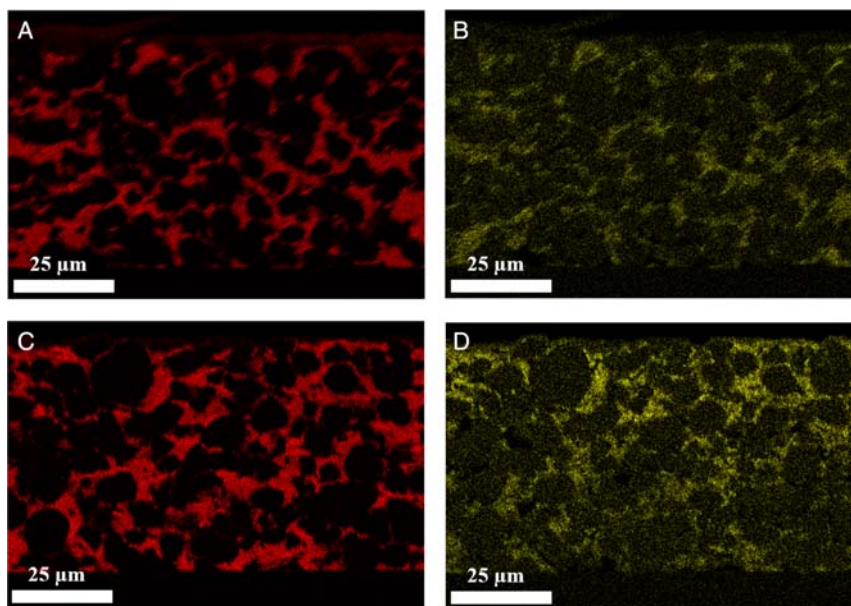


Figure 9. A,C) Carbon and B,D) fluorine EDS mapping of calendered NCM-C for drying rates of $0.75 \text{ g m}^{-2} \text{ s}^{-1}$ (A,B) and $3.5 \text{ g m}^{-2} \text{ s}^{-1}$ (C,D).

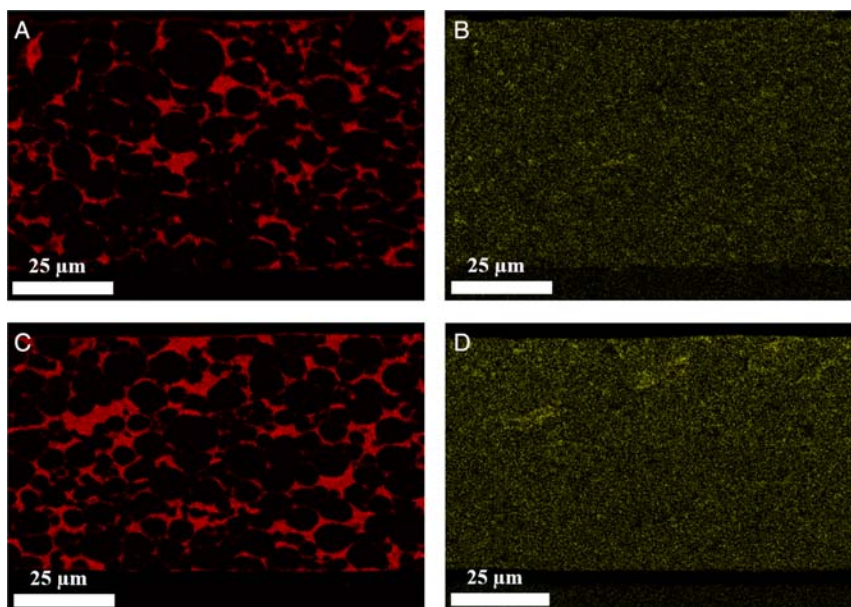


Figure 10. A,C) Carbon and B,D) fluorine distributions of calendared NCM-P for a drying rate of $0.75 \text{ g m}^{-2} \text{ s}^{-1}$ (A,B) and $3.5 \text{ g m}^{-2} \text{ s}^{-1}$ (C,D).

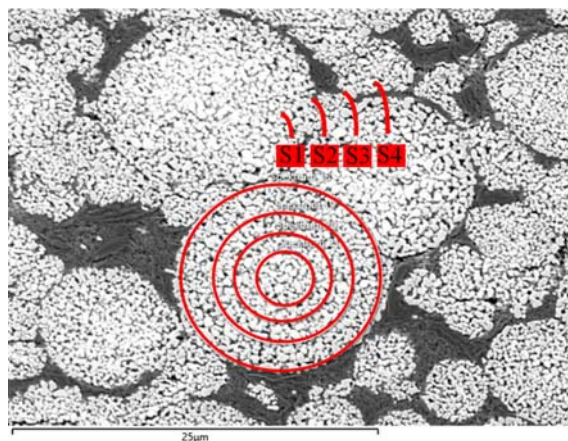


Figure 11. SEM image of secondary particles in cross section of dried NCM-P cathode with marked areas for EDS analysis of fluorine concentration.

Table 5. Fluorine distribution within secondary particles in cross section of dried NCM-P cathodes at low and high drying rate (0.75 and $3.5 \text{ g m}^{-2} \text{ s}^{-1}$).

Spectrum	Fluorine concentration [at%] Drying rate $0.75 \text{ g m}^{-2} \text{ s}^{-1}$	Fluorine concentration [at%] Drying rate $3.5 \text{ g m}^{-2} \text{ s}^{-1}$
S1	2.29	2.48
S2	2.64	2.78
S3	2.68	2.68
S4	2.64	2.68

This indicates that the interparticle pores are already emptied before the drying of the intraparticle pores of the NCM-P starts and substantial capillary transport does not take place out of the

secondary particles. This can cause the solvent present in the secondary particles to withdraw into the secondary particles during evaporation and to be transported via the gas phase within the drying electrode. The retention of binder within the particles until the end of electrode drying leads to an imposed more homogeneous binder distribution in the electrode cross section.

Due to a comparatively lower proportion of binder and, thus, conductive binder bridges near the current collector of the electrode, the amount of contact points between the active materials and the current collector decreases.^[12,40] If the binder concentration near the current collector decreases with increasing drying rate, the adhesion decreases and the resistivity increases. In the case of the NCM-P particles, the binder content is reduced near the current collector and decreases only minimally with increasing drying rate. This could explain the smaller increase in electrical resistivity with increasing drying rate.

2.7. Sequential Drying Mechanism of Slurries with Porous, Nanostructured Particles

Based on the findings, a sequential drying mechanism is proposed to understand and illustrate the drying of electrodes with porous active material particles. This is based on the literature presented and has been extended to include the intrinsic particle morphology of NCM-P.

Accordingly, the NCM-P particles are filled with solvent and the dissolved PVDF binder at the beginning of drying. With increasing solvent removal during drying, the secondary particles approach each other until the end of film shrinkage is reached (Figure 12A). At this point the entire porosity of the electrode is still filled with solvent.

As drying progresses, pore emptying of the large interparticle pores between the particles begins. This is accomplished by capillary transport through smaller pores to the electrode surface.

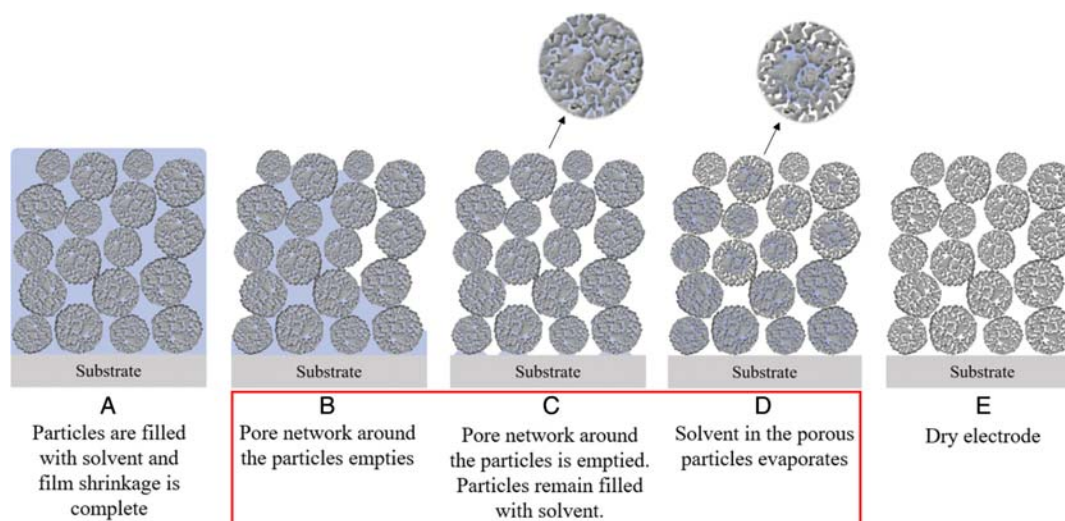


Figure 12. Schematic representation of the drying process of a particulate film with porous, nanostructured particles. For simplification, only the porous particles and the solvent are shown here. In reality, phases B–D are not strictly separated, but for the most run in parallel. Emptying of porous particles starts directly, when surrounding interparticle pores are emptied, since both stages represent equal conditions for heat and mass transfer.

The smaller intraparticle pores within the particles do not empty to the larger interparticle pores due to their much higher capillary pressure. With the film at steady-state temperature, the resistance of mass transfer is controlled on the gas side and the evaporation rate depends on the vapor pressure of the solvent at the liquid surface, the mass transport coefficient and the solvent loading in the drying air. As long as the drying rate is maintained by sufficient liquid wetting at the top of the electrode, this drying section is also described as a constant rate period (CRP), characterized by a steady state with a constant drying rate (Figure 12B). Initiated by the capillary liquid transport, the binder will also be transported to the top of the electrode. The film height no longer changes significantly in this stage.

With decreasing mass flux of evaporating solvent, the falling rate period begins. Once sufficiently large pores are empty, the gas-liquid interface retreats into the interior of the electrode, because the capillary forces are no longer able to transport the liquid to the surface due to insufficient solvent content and due to high capillary pressure (Figure 12B,C). If a nearby interparticle pore is empty, the solvent can also evaporate from within a secondary particle (Figure 12D). However, as long as the particle has contact with another solvent filled interparticle pore, the solvent loss will be compensated by wicking. Drying of a secondary particle starts when all adjacent interparticle pores are empty.

In that case, the drying mechanism is hypothesized to be an evaporation front, progressing gradually into the particles, based on the absence of an interparticle binder gradient (Figure 11). This hypothesis is supported by the fact that the pore size distribution within the secondary particles is very narrow,^[12] resulting in slight capillary pressure differences within the particles. There is an additional transport resistance for heat and mass transfer in that final step, which is why the drying rate is controlled by the gas and the film side. The temperature of the electrode increases as time progresses and approaches the temperature of the gas phase (Figure 12C–E). The drying process is complete when all solvent is removed from within the secondary particles

(Figure 12E). In this state, the whole electrode has achieved the temperature of the gas phase.

2.8. Electrochemical Performance

The resistance increase, caused in particular by the non-uniform distribution of the components due to binder migration, has an effect on the potential curve and the discharge capacity at higher currents or C-rates.^[18,34–36] To investigate the influence of drying conditions and different degree of binder migration on the electrochemical properties of the cathodes, half cells were cycled at different C rates (Figure 13).

For the most part, uncalendered cathodes with NCM-P exhibit higher discharge capacities than cathodes made of NCM-C at both low and high drying rates. At 1C and the lowest drying rate, the capacity of NCM-P at $143.41 \pm 1.48 \text{ mAh g}^{-1}$ is about 8% higher than that of NCM-C at $132.56 \pm 1.28 \text{ mAh g}^{-1}$. Due to the high electrode porosity and the electrical resistivity of NCM-P, these performance differences were not expected. It is possible that in the porous, structured system the ionic resistances are the limiting resistances for the electrochemical performance, which is why NCM-P exhibits higher discharge capacities in the uncalendered state.

By calendering the layers with porous, structured particles, a capacity of $85.36 \pm 4.03 \text{ mAh g}^{-1}$ at 5C could be achieved for the highest drying rate and is thus 54% higher than in the uncalendered state ($55.34 \pm 1.96 \text{ mAh g}^{-1}$). Compared to the calendered electrode at 5C with NCM-C ($36.67 \pm 5.52 \text{ mAh g}^{-1}$) at the highest drying rate, the capacity is 133% higher for electrodes with NCM-P.

Increasing the drying rate results in a worse C-rate capability for NCM-C. At a C rate of 5C, the discharge capacity has dropped by $\approx 63\%$. The evolution of the discharge capacities of NCM-C at higher C-rates correspond to the inverse evolution of the electrical resistivity with increasing drying rate. A much lower

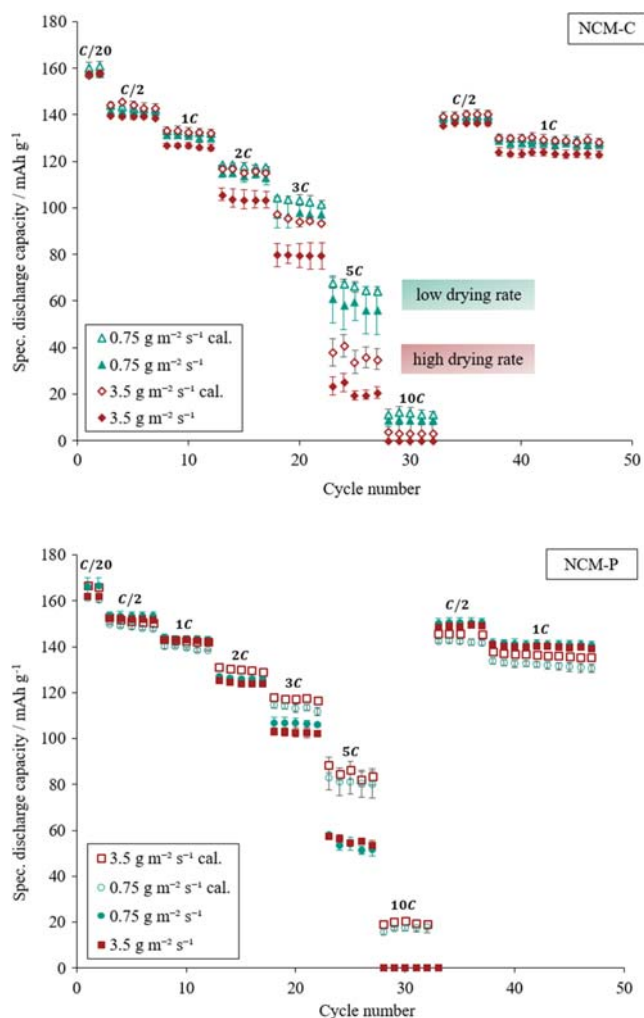


Figure 13. Specific discharge capacities of half cells at varying C rates. Comparison of uncalendered and calendered cathodes with NCM-C and NCM-P dried at a drying rate of 0.75 and 3.5 $\text{g m}^{-2} \text{s}^{-1}$ at a constant heat transfer coefficient of $80 \text{ W m}^{-2} \text{ K}^{-1}$. The discharge capacities show no dependence on the drying rate for electrodes made of porous, structured particles.

dependence of C-rate capability due to an increase in drying rate is present for NCM-P. At a C-rate of 3C, the discharge capacity is 3.8% higher at the lower drying rate than at the higher drying rate. At 5C, the discharge capacities overlap as the number of cycles increases.

The strongly pronounced binder concentration gradient with increasing drying rate shown, could lead to an increase in resistivities for NCM-C, resulting in a decrease in C-rate stability. In addition to the electrical resistivity, an accumulation of the binder on the surface of the active material in the upper region of the electrode could increase the charge transfer resistance and enlarge the tortuosity of the lithium ions within the electrode porosity due to a reduced active exchange surface (ionic resistivity). These resistances increase the overpotential within the cell, the cut-off voltage is reached earlier, resulting in the lower discharge capacities for NCM-C at higher drying rates. Thus,

electrodes made of NCM-P particles show less dependence on the drying process at the present slurry configuration and under the manufacturing conditions, which is due to the less pronounced binder migration combined with an overall higher specific surface area of active material.

3. Conclusion

In this work, the drying behavior of NCM cathode electrodes for lithium-ion batteries with compact (NCM-C) and porous, structured (NCM-P) particles was investigated. Starting from the battery slurries, the dependence of particle morphology and drying conditions on mechanical, electrical, and electrochemical properties was compared. For this purpose, electrodes were prepared from cathode slurries of the same composition with the respective active materials under different drying rates. The solvent and the binder dissolved in the slurry penetrates the open porosity of the NCM-P particles and leads to an increase of the effective solids volume fraction. By this, the viscosity is higher over the entire shear rate range than for a slurry with compact NCM particles.

Evaluation of EDS images show increased migration of PVDF binder to the top of the electrodes for cathodes with NCM-C when the drying rate is increased, resulting in a decrease in adhesion force as well as an increase in electrical resistance. For NCM-P and for the slurry composition used, the binder migration is less pronounced with increasing drying rate. The cause of this is assumed to be a different drying mechanism due to the connection between binder migration and capillary solvent transport.

The investigation of binder gradients of the porous active material particles indicates that in the porous, nanostructured particles themselves no significant capillary transport takes place due to excessive capillary pressure. With regard to the drying behavior of NCM-P, it is hypothesized that initially the outer pore network around the porous particles is dried by capillary transport effects and the subsequent drying of the porous active material particles takes place through individual evaporation fronts.

It is likely that the significantly lower increase in electrical resistivity of NCM-P is directly related to the less pronounced binder migration. The resistivity data of NCM-P are higher than those of NCM-C by a factor of 5–10. The adhesion force with NCM-P is lower by a factor of up to 7 than with NCM-C.

Half-cell tests on uncalendered cathodes show that an increase in the drying rate for NCM-C leads to a decreasing C-rate capability due to an increasing overpotential. This is correlated with the higher electrical resistance caused by the higher binder concentration in the upper area of the electrode. Presumably, the charge transfer resistance also increases. Despite the higher electrical resistance, uncalendered cathodes made of porous, nanostructured particles show higher discharge capacities with a better C-rate capability. With regard to processing, there is also the experience that the electrochemical properties of the NCM-P electrodes show little dependence on the drying rate. This is attributed to the less pronounced binder migration and the larger electrochemically active surface. As a result, cathodes with NCM-P can be dried with higher drying rates and, thus, enable

shorter drying time without any significant loss of mechanical properties and electrochemical performance.

In order to improve the mechanical properties of electrodes with porous, nanostructured active materials in the future, the use of multilayer electrodes with different binder contents in the individual layers or a very thin primer layer should be investigated. A multilayer electrode consisting of a lower layer with solid particles and an upper layer with porous, nanostructured particles could lead to an improvement of the adhesive force by simultaneously maintaining beneficial electrochemistry. For a specific optimization of the electrodes, investigations and the understanding of the processing of such multilayer systems made of different compositions and different active materials are necessary. For a more detailed linking of the mechanical and electrical properties with the electrochemical performance as a function of the particle systems and the drying rate, electrochemical impedance measurements should be performed.

4. Experimental Section

Slurry Materials and Mixing: The slurry for NCM-C (NM-3100, Toda Kogyo Corp.) and NCM-P cathodes were mixed in a dissolver (Dispermat SN-10, VMA Getzmann/Germany). The conductive additives carbon black Super C65 (Imerys) and graphite KS6L (Imerys), a PVDF Solef 5130 (Solvay) binder solvent solution (7.5 wt%) and about 50% of the required amount of NMP (Carl Roth, Germany) were dispersed at 1000 rpm for 30 min. The active material was added with the remaining NMP to adjust the solid content (50.5 wt%) and dispersed at 1000 rpm for 30 min.

The viscosity was measured by a rotation viscometer Physica MCR 101 (Anton Paar, Germany) in plate-plate system with 25 mm diameter from 0.01 to 1 000 s⁻¹ at 25 °C.

Electrode Coating and Drying: The coating and drying of the cathode electrodes was carried out as a discontinuous process. The aluminum foil (Schlenk, 20 μm) was attached to a temperature-controlled plate. The coating of the cathode slurries was applied with a doctor blade ZUA 2000.60 (Zehntner) and subsequently the coating was run under the drying nozzles of an impingement dryer. For homogeneous drying, the coating is periodically moved under the dryer until the electrode was dry.

Electrodes Characterization: To determine the adhesion force between the substrate and the dried electrodes, a 90° peel test was carried out (Zwick, 10 N load cell). Sample strips of the dried cathodes were cut out with a width of 17 mm and attached with the coated side to an adhesive strip. The current collector foil was then peeled off the coating at a constant speed of 600 mm min⁻¹ at a 90° angle using the testing machine. The resulting pull-off force was measured and divided by the sample width to obtain a line adhesive force.

The electrical resistance was determined with an ohmmeter (HIOKI, RM3544). For this purpose, circular samples of the cathodes placed between polished copper cylinders with a diameter of 14 mm and a force of 9.81 N.

SEM/EDS: A Zeiss Supra 55 from Carl Zeiss AG (Oberkochen, Germany) was used for SEM investigations. An Ultim Extreme detector from Oxford Instruments plc (Abingdon, UK) was used to perform EDS measurements.

Half Cell Preparation: The cathodes were electrochemically examined in coin cells against a lithium-metal counter electrode. The electrolyte used was 200 μL LP30 (BASF) with the conductive salt 1 M LiPF₆ in an EC/DMC (1:1) mixture. The separator was a glass microfiber fleece (GF/C, Whatman) with a diameter of 16 mm. The cells were assembled in a glove-box and sealed with a MSK-11 press (MTI, KJ Group).

Cell Tests: The cycling was carried out in a BT2000 battery cycler from Arbin Instruments in constant current mode in a voltage window of 3 to 4.3 V. Identical C-rates were used for charging and discharging. After two

formation cycles at a C-rate of C/20, the C-rate was gradually increased to 10C. Two more steps were carried out, at C/2 and 1C.

Acknowledgements

This work contributes to the research performed at CELEST (Center for Electrochemical Energy Storage Ulm Karlsruhe) and Material Research Center for Energy Systems (MZE). It was funded by the Deutsche Forschungsgemeinschaft (DFG, German Research Foundation) under Germany's Excellence Strategy – EXC 2154 – Project number 390874152 (POLiS Cluster of Excellence). The authors would like to thank the assistants involved in this work: Thilo Heckmann, Victor Alfonso Gracia-Medrano-Bravo, Sandro Spiegel.

Open access funding enabled and organized by Projekt DEAL.

Conflict of Interest

The authors declare no conflict of interest.

Data Availability Statement

The data that support the findings of this study are available from the corresponding author upon reasonable request.

Keywords

binder migration, drying, electrode processing, lithium-ion batteries, NCM, particle morphologies

Received: November 5, 2021

Revised: January 3, 2022

Published online:

- [1] Y. Zhao, O. Pohl, A. I. Bhatt, G. E. Collis, P. J. Mahon, T. Rüter, A. F. Hollenkamp, *Sustainable Chem.* **2021**, *2*, 167.
- [2] D. Ren, E. Padgett, Y. Yang, L. Shen, Y. Shen, B. D. A. Levin, Y. Yu, F. J. DiSalvo, D. A. Muller, H. D. Abruña, *ACS Appl. Energy Mater.* **2019**, *11*, 41178.
- [3] M. Jiang, Q. Zhang, X. Wu, Z. Chen, D. L. Danilov, R.-A. Eichel, P. H. L. Notten, *ACS Appl. Energy Mater.* **2020**, *3*, 6583.
- [4] Z. Yang, J. Lu, D. Bian, W. Zhang, X. Yang, J. Xia, G. Chen, H. Gu, G. Ma, *J. Power Sources* **2014**, *272*, 144.
- [5] L. Li, L. Wang, X. Zhang, M. Xie, F. Wu, R. Chen, *ACS Appl. Mater. Interfaces* **2015**, *7*, 21939.
- [6] B. Lin, Z. Wen, Z. Gu, S. Huang, *J. Power Sources* **2008**, *175*, 564.
- [7] Z.-D. Huang, X.-M. Liu, S.-W. Oh, B. Zhang, P.-C. Ma, J.-K. Kim, *J. Mater. Chem.* **2011**, *21*, 10777.
- [8] M. Oljaca, B. Blizanac, A. Du Pasquier, Y. Sun, R. Bontchev, A. Suszko, R. Wall, K. Koehler, *J. Power Sources* **2014**, *248*, 729.
- [9] A. C. Wagner, N. Bohn, H. Geßwein, M. Neumann, M. Osenberg, A. Hilger, I. Manke, V. Schmidt, J. R. Binder, *ACS Appl. Energy Mater.* **2020**, *3*, 12565.
- [10] A. M. Dreizler, N. Bohn, H. Geßwein, M. Müller, J. R. Binder, N. Wagner, K. A. Friedrich, *J. Electrochem. Soc.* **2018**, *165*, A273.
- [11] Y. Su, Q. Zhang, L. Chen, L. Bao, Y. Lu, Q. Shi, J. Wang, S. Chen, F. Wu, *ChemSusChem* **2020**, *13*, 426.
- [12] M. Müller, L. Schneider, N. Bohn, J. R. Binder, W. Bauer, *ACS Appl. Energy Mater.* **2021**, *4*, 1993.
- [13] S. Jaiser, L. Funk, M. Baunach, P. Scharfer, W. Schabel, *J. Colloid Interface Sci.* **2017**, *494*, 22.

- [14] S. Jaiser, J. Kumberg, J. Klaver, J. L. Urai, W. Schabel, J. Schmatz, P. Scharfer, *J. Power Sources* **2017**, 345, 97.
- [15] J. Kumberg, M. Müller, R. Diehm, S. Spiegel, C. Wachsmann, W. Bauer, P. Scharfer, W. Schabel, *Energy Technol.* **2019**, 7, 1900722.
- [16] M. Müller, L. Pfaffmann, S. Jaiser, M. Baunach, V. Trouillet, F. Scheiba, P. Scharfer, W. Schabel, W. Bauer, *J. Power Sources* **2017**, 340, 1.
- [17] L. Pfaffmann, S. Jaiser, M. Müller, P. Scharfer, W. Schabel, W. Bauer, F. Scheiba, H. Ehrenberg, *J. Power Sources* **2017**, 363, 460.
- [18] S. Jaiser, M. Müller, M. Baunach, W. Bauer, P. Scharfer, W. Schabel, *J. Power Sources* **2016**, 318, 210.
- [19] M. Baunach, S. Jaiser, S. Schmelzle, H. Nirschl, P. Scharfer, W. Schabel, *Drying Technol.* **2016**, 34, 462.
- [20] L. S. Kremer, A. Hoffmann, T. Danner, S. Hein, B. Prifling, D. Westhoff, C. Dreer, A. Latz, V. Schmidt, M. Wohlfahrt-Mehrens, *Energy Technol.* **2020**, 8, 1900167.
- [21] V. Gnielinski, A. Mersmann, F. Thurner, *Verdampfung, Kristallisation, Trocknung*, Springer Berlin Heidelberg, Berlin, Heidelberg, s.l., **1993**.
- [22] O. Krischer, *Die Wissenschaftlichen Grundlagen Der Trocknungstechnik*, Springer Berlin Heidelberg, Berlin, Heidelberg, s.l., **1963**.
- [23] E.-U. Schlünder, *Drying Technol.* **2004**, 22, 1517.
- [24] E.-U. Schlünder, *Chem. Ing. Tech.* **1988**, 60, 117.
- [25] S. Jaiser, N. Sanchez Salach, M. Baunach, P. Scharfer, W. Schabel, *Drying Technol.* **2017**, 35, 1807.
- [26] G. W. Scherer, *J. Am. Ceram. Soc.* **1990**, 73, 3.
- [27] T. Metzger, E. Tsotsas, *Drying Technol.* **2005**, 23, 1797.
- [28] R. Morasch, J. Landesfeind, B. Suthar, H. A. Gasteiger, *J. Electrochem. Soc.* **2018**, 165, A3459.
- [29] F. Font, B. Protas, G. Richardson, J. M. Foster, *J. Power Sources* **2018**, 393, 177.
- [30] S. Lim, K. H. Ahn, M. Yamamura, *Langmuir* **2013**, 29, 8233.
- [31] H. Hagiwara, W. J. Suszynski, L. F. Francis, *J. Coat. Technol. Res.* **2014**, 71, 11.
- [32] W. B. Hawley, J. Li, *J. Energy Storage* **2019**, 25, 100862.
- [33] S. N. Bryntesen, A. H. Strømman, I. Tolstorebrov, P. R. Shearing, J. J. Lamb, O. Stokke Burheim, *Energies* **2021**, 14, 1406.
- [34] B. Westphal, H. Bockholt, T. Gunther, W. Haselrieder, A. Kwade, *ECS Trans.* **2015**, 64, 57.
- [35] J. Kumberg, W. Bauer, J. Schmatz, R. Diehm, M. Tönsmann, M. Müller, K. Ly, P. Scharfer, W. Schabel, *Energy Technol.* **2021**, 9, 2100367.
- [36] R. Diehm, J. Kumberg, C. Dörrer, M. Müller, W. Bauer, P. Scharfer, W. Schabel, *Energy Technol.* **2020**, 8, 1901251.
- [37] J. Kumberg, M. Baunach, J. C. Eser, A. Altvater, P. Scharfer, W. Schabel, *Energy Technol.* **2021**, 9, 2100013.
- [38] W. Bauer, D. Nötzel, *Ceram. Int.* **2014**, 40, 4591.
- [39] R. Diehm, H. Weinmann, J. Kumberg, M. Schmitt, J. Fleischer, P. Scharfer, W. Schabel, *Energy Technol.* **2020**, 8, 1900137.
- [40] R. Diehm, M. Müller, D. Burger, J. Kumberg, S. Spiegel, W. Bauer, P. Scharfer, W. Schabel, *Energy Technol.* **2020**, 8, 2000259.
- [41] G. Liu, H. Zheng, X. Song, V. S. Battaglia, *J. Electrochem. Soc.* **2012**, 159, A214.
- [42] J. Landesfeind, A. Eldiven, H. A. Gasteiger, *J. Electrochem. Soc.* **2018**, 165, A1122.
- [43] T. Marks, S. Trussler, A. J. Smith, D. Xiong, J. R. Dahn, *J. Electrochem. Soc.* **2011**, 158, A51.
- [44] G. Liu, H. Zheng, S. Kim, Y. Deng, A. M. Minor, X. Song, V. S. Battaglia, *J. Electrochem. Soc.* **2008**, 155, A887.